

The formation of CDM haloes I: Collapse thresholds and the ellipsoidal collapse model

Aaron D. Ludlow^{*}, Mikolaj Borzyszkowski & Cristiano Porciani

Argelander-Institut für Astronomie, Auf dem Hügel 71, D-53121 Bonn, Germany

11 November 2018

ABSTRACT

In the excursion set approach to structure formation initially spherical regions of the linear density field collapse to form haloes of mass M at redshift z_{id} if their linearly extrapolated density contrast, averaged on that scale, exceeds some critical threshold, $\delta_c(z_{\text{id}})$. The value of $\delta_c(z_{\text{id}})$ is often calculated from the spherical or ellipsoidal collapse model, which provide well-defined predictions given auxiliary properties of the tidal field at a given location. We use two cosmological simulations of structure growth in a Λ cold dark matter scenario to quantify $\delta_c(z_{\text{id}})$, its dependence on the surrounding tidal field, as well as on the shapes of the Lagrangian regions that collapse to form haloes at z_{id} . Our results indicate that the ellipsoidal collapse model provides an accurate description of the mean dependence of $\delta_c(z_{\text{id}})$ on both the strength of the tidal field and on halo mass. However, for a given z_{id} , $\delta_c(z_{\text{id}})$ depends strongly on the halo’s characteristic formation redshift: the earlier a halo forms, the higher its initial density contrast. Surprisingly, the majority of haloes forming *today* fall below the ellipsoidal collapse barrier, contradicting the model predictions. We trace the origin of this effect to the non-spherical shapes of Lagrangian haloes, which arise naturally due to the asymmetry of the linear tidal field. We show that a modified collapse model, that accounts for the triaxial shape of protohaloes, provides a more accurate description of the measured minimum overdensities of recently collapsed objects.

Key words: gravitation – methods: numerical – galaxies: haloes – cosmology: theory – dark matter.

1 INTRODUCTION

In the standard model for the growth of large-scale structure, cold dark matter (CDM) haloes form hierarchically from low-amplitude Gaussian density fluctuations seeded during inflation. As the Universe expands, sufficiently overdense regions eventually break away from the Hubble flow, recollapse and form virialized objects. Due to their highly non-linear nature, these objects are best studied using direct N -body simulation, and dedicated numerical work has revolutionized our understanding of the most fundamental aspects of their formation, evolution and structure. Never the less, simulations are often difficult to interpret and insight into the rudimentary principles of structure formation can be significantly enhanced by supplementing them with simple physical models for the collapse and virialization of dark matter (DM) haloes.

One successful analytic approach to modelling structure formation, known as the Extended Press-Schechter formalism (e.g., Press & Schechter 1974; Bond et al. 1991,

hereafter EPS), relates the (Eulerian) statistics of DM haloes to the properties of the Lagrangian density field from which they emerge. Although Press & Schechter (1974) originally used this model to calculate the mass function of collapsed objects at different redshifts, it has since been extended and used to compute a variety of hierarchical clustering statistics, such as halo merger histories (e.g., Kauffmann & White 1993; Lacey & Cole 1993; Sheth & Lemson 1999b; van den Bosch 2002), and spatial correlations (Mo & White 1996; Mo et al. 1997; Catelan et al. 1998; Porciani et al. 1998; Sheth & Lemson 1999a).

The accuracy of the model is surprising given that it overlooks a variety of non-linear and scale-dependent aspects of gravitational clustering. Regarding structure formation, its simplicity is also its strength: it provides an intuitive picture of a much more complex process, and can help to guide and interpret more sophisticated numerical calculations of structure growth.

One of the principal assumptions of EPS theory (also known as the excursion-set formalism) is the idea that a mass element at position \mathbf{x} at some high initial redshift

^{*} E-mail: aludlow@astro.uni-bonn.de

$z_i \gg 0$ will be associated with a halo of mass M at some later redshift, z_c , provided its linear overdensity, $\delta_M(\mathbf{x}, z_c)$ (smoothed on scale M and extrapolated to that redshift by linear theory), exceeds a threshold B . For an initial overdensity $\delta_M(\mathbf{x}, z_i)$ at redshift z_i , collapse therefore occurs provided

$$\delta_M(\mathbf{x}, z_i) \frac{D(z_c)}{D(z_i)} = B(z_c) \quad (1)$$

is satisfied, where $D(z)$ is the growth factor of linear perturbations.

The collapse “barrier”, B , however, is not known a priori, and one must gain insight from simple dynamical models for gravitational collapse. The spherical collapse (SC) model (Peebles 1980), for example, follows the evolution of a sphere of constant overdensity in an otherwise unperturbed but expanding background. This model is patently scale-free and (for a given collapse redshift, z_c) the barrier therefore depends only on the local density, $B(z_c) \equiv \delta_{\text{sc}}(z_c) \approx 1.686$. Although this result is derived for an Einstein–de Sitter universe, it is approximately valid for a large range of cosmologies. Eke et al. (1996) provide useful analytic corrections to the value of δ_{sc} for cosmologies with $\Omega_M + \Omega_\Lambda = 1$.

White (1996) pointed out that EPS theory, combined with the SC threshold, fails when applied on a point-by-point basis. Using N -body simulations, they showed that the largest mass associated with a Lagrangian overdensity δ_{sc} at random particle locations correlates poorly with the mass of the halo in which the same particles were found at $z = 0$. A significant improvement can be made, however, by considering the Lagrangian locations \mathbf{x}_h of “protohaloes” – regions that later collapse to form haloes – rather than random points. However, even with this input from simulations, the SC barrier, $B = \delta_{\text{sc}}$, still systematically over-predicts the corresponding halo masses (Sheth et al. 2001), with a discrepancy that increases towards lower mass.

It is well-known that perturbations in Gaussian random fields are inherently triaxial and are therefore subject to tidal forces (Doroshkevich 1970; Bardeen et al. 1986). This motivated attempts to modify the spherical model to incorporate the influence of tides on halo collapse. Building upon the classic work of Lynden-Bell (1964) and Lin et al. (1965), a number of authors studied the effect of internal shear on the collapse of homogeneous ellipsoids in a uniformly expanding background (e.g., Icke 1973; White & Silk 1979; Peebles 1980; Watanabe & Inagaki 1991; Lemson 1993). Eisenstein & Loeb (1995) and (Bond & Myers 1996, hereafter BM96) generalized this model to follow the collapse of an initially spherical perturbation in the presence of external shear. In this case, the sphere is distorted into an ellipsoid whose principal axes are parallel to those of the external tidal field. This model has since become known as the ellipsoidal collapse model (hereafter, the EC model) due to the triaxiality of both the tidal field and the collapsing ellipsoid itself. Using this model one can ascertain the impact of tidal shear on the properties of collapsed regions.

The tidal stretching and compression of initially spherical perturbations in the EC model results in a barrier height that depends on all three eigenvalues of the tidal deformation tensor at \mathbf{x} . Sheth et al. (2001) realized that the ellipsoidal barrier, combined with the statistical properties of Gaussian random fields, implied that fluctuations of lower

mass should be subject to larger degrees of tidal deformation. They used this to approximate the dependence of B on halo mass and showed that, when properly tuned, the EC model employed within the excursion-set formalism provides a more accurate description of the abundance of DM haloes, as well as the statistical properties of their progenitor populations (Sheth & Tormen 2002).

Using cosmological simulations of structure growth, Robertson et al. (2009, see also Dalal et al. 2008; Elia et al. 2012) measured the Lagrangian overdensities of regions which later collapse to form haloes of mass M , and found a $\delta(M)$ relation that resembled the expectations of the EC model, suggesting that it captures the most relevant aspects of gravitational collapse. None the less, when adopting the ellipsoidal collapse barrier and the excursion set ansatz for random points, they failed to provide an accurate prediction of the DM halo mass function. Indeed, the success of the ellipsoidal model in predicting the Eulerian statistics of the DM halo population is not based on a direct application of B_{ec} within the EPS theory. Instead, a functional form for B_{ec} (whose *shape* is motivated by the EC model) is determined and calibrated directly against the measurable halo statistic that one wishes to predict. Sheth et al. (2001), for example, rescaled the EC barrier in order to reproduce the mass function of DM haloes obtained from numerical simulations. It is therefore important to critically investigate the EC model and the excursion set ansatz separately, in order to assess whether the SC or EC models themselves provide a reasonable physical picture of halo formation.

The purpose of this paper is to investigate the statistical properties of Lagrangian DM haloes (or protohaloes) found in N -body simulations of structure growth and to compare them with the expectations of the spherical and ellipsoidal collapse models. The remainder of the paper is organized as follows. In Section 2 we introduce our simulations and briefly describe our main analysis techniques. The basic characteristics of protohaloes in our simulations are presented in Section 3, focusing mainly on their Lagrangian overdensities and surrounding tidal fields. Motivated by those results, we present a modified EC model in Section 4. Finally, we provide a brief discussion and summary of our findings in Sections 5 and 6.

2 NUMERICAL METHODS

We present here a brief summary of our numerical simulations. More details can be found in Pillepich et al. (2010) and Ludlow & Porciani (2011).

2.1 Simulations

Our analysis focuses primarily on DM haloes extracted from two high-resolution simulations of structure formation in the standard Λ CDM cosmology. Each run adopted the following cosmological parameters: $\Omega_M = 0.279$, $\Omega_\Lambda = 1 - \Omega_M = 0.721$, $\sigma_8 = 0.817$, $n_s = 0.96$, and $H_0 \equiv H(z = 0) = 73 \text{ km s}^{-1} \text{ Mpc}$, consistent with those of the *Wilkinson Microwave Anisotropy Probe* five-year data release (Komatsu et al. 2009). Here Ω_i is the contribution to the total energy density of the Universe from component i ; σ_8 is the rms mass fluctuation measured in $8 h^{-1} \text{ Mpc}$

spheres, linearly extrapolated to $z = 0$; n_s is the spectral index of primordial density fluctuations, and H_0 is Hubble's constant.

The linear density fields for each run were sampled using 1024^3 equal-mass particles in periodic boxes with side-lengths equal to $l_{\text{box}} = 150$ and $1200 h^{-1}$ Mpc. For these choices of cosmological parameters, box sizes, and particle number the particle masses are 2.433×10^8 and $1.246 \times 10^{11} h^{-1} M_\odot$ in the 150 and $1200 h^{-1}$ Mpc boxes, respectively. The corresponding softening lengths are 3 and $20 h^{-1}$ kpc, which are kept fixed in comoving coordinates throughout the simulations.

Initial conditions for our simulations were generated by perturbing the initially uniform distribution of particles using the Zel'dovich approximation consistent with a starting redshift of $z_i = 70$ for the $150 h^{-1}$ Mpc box and $z_i = 50$ for the $1200 h^{-1}$ Mpc box. As discussed by Pillepich et al. (2010), these redshifts are sufficiently high so that possible transient features in the halo mass function are effectively erased by $z \approx 2$. For each simulation, 30 snapshots of the particle distribution were saved between $z = 10$ and 0 in equally spaced steps of $\log(1+z)^{-1}$.

2.2 Halo and Protohalo Catalogues

In each run, DM haloes were identified in all 30 simulation outputs using a friends-of-friends (FoF) halo finder with a link length of 0.2 times the mean nearest-neighbour spacing. We retain the identities of all FoF haloes that contain more than 32 particles but, in what follows, we restrict our analysis to those having at least $N_{\text{min}} = 500$. We have verified that our results are insensitive to our particular choice of halo finder by repeating the most pertinent aspects of the analysis using DM haloes identified with a spherical-overdensity halo finder that adopted a density contrast of 200 times the mean matter density, ρ_m .

Our analysis focuses on DM haloes identified at four separate redshifts: $z_{\text{id}} = 0, 1, 2$ and 3. For all haloes identified at z_{id} we construct accretion histories by tracing their most massive progenitor haloes backwards through all previous simulation outputs. We will use z_{50} , the redshift at which the most massive progenitor had first assembled 50 per cent of its descendants mass at z_{id} , as a proxy for each halo's formation redshift. Our estimates of z_{50} are obtained by linearly interpolating the mass accretion histories between simulation snapshots and we have verified that, over the mass and redshift ranges studied here, they are not unduly influenced by our output sequence. In what follows we will refer to this redshift as z_{50} , in order to distinguish it from a more general ‘collapse’ redshift, z_c ; the corresponding cosmological times will be referred to as t_{50} , t_c and t_{id} .

DM protohaloes are defined as the Lagrangian patches in the linear density field that are occupied by the subset of particles belonging to each FoF halo at z_{id} . The mass of a protohalo is therefore equal to the mass of its descendant at z_{id} .

2.3 Analysis

We measure protohalo shapes using the following description of their mass distribution (e.g., Cole & Lacey 1996;

Bailin & Steinmetz 2005; Bett et al. 2007):

$$I_{ij} = \sum_k \frac{x_{k,i} x_{k,j}}{x_k^2}, \quad (2)$$

where x_k is the distance to particle k from the protohalo's centre of mass; and i and j are the components of \mathbf{x} along the Cartesian axes of the simulation. The factor of $1/x_k^2$ is present in equation (2) to prevent particles at large distances from dominating the shape estimates, but in practice our results are insensitive to this weighting. This matrix can be diagonalized and the principal axis lengths, $q_1 \geq q_2 \geq q_3$, determined from the square roots of its eigenvalues; the eigenvectors, \mathbf{i}_i , define the principal axis frame of the system. Once the axis lengths q_i have been found, protohalo shapes can be characterized in terms of their ratios: q_2/q_1 measures the intermediate-to-major axis ratio, and q_3/q_1 the minor-to-major axis ratio.

In addition to shapes, we also measure properties of the tidal field in the vicinity of each protohalo using the tidal deformation tensor, defined

$$\mathcal{D}_{ij} = \frac{\partial^2 \Phi}{\partial x_i \partial x_j}. \quad (3)$$

Here $\Phi(\mathbf{x})$ is the peculiar gravitational potential at position \mathbf{x} , which is related to the density contrast by Poisson's equation: $\nabla^2 \Phi(\mathbf{x}) = \delta(\mathbf{x})$. Note that, in practice, all fields are evaluated in Fourier space. By diagonalizing \mathcal{D} we obtain its ordered eigenvalues, $\lambda_1 \geq \lambda_2 \geq \lambda_3$; these determine the geometry of the tidal field at \mathbf{x} , and their sign indicates whether the flow is inward (+) or outwards (−). The eigenvectors of \mathcal{D} , \mathbf{d}_i , determine the orientation of the flow. At any time, \mathbf{d}_1 points along the direction of maximum compression; \mathbf{d}_3 aligns with the axis of minimum compression (or expansion). Note that $\delta(\mathbf{x}) = \sum_i \lambda_i(\mathbf{x})$, so the tidal field contains all information necessary to construct linear overdensities at \mathbf{x} .

It is common to express the eigenvalues of \mathcal{D} in terms of the ellipticity, e , and prolateness, p , of the tidal field. These are defined by

$$e = \frac{\lambda_1 - \lambda_3}{2\delta} \quad (4)$$

and

$$p = \frac{\lambda_1 - 2\lambda_2 + \lambda_3}{2\delta}. \quad (5)$$

The combination of (e, p, δ) or $(\lambda_1, \lambda_2, \lambda_3)$ therefore provide an equivalent description of the linear tidal field.

3 PROTOHALOES IN COSMOLOGICAL SIMULATIONS

3.1 Overdensities

The EC model makes specific predictions for the linear overdensity required for collapse to occur at redshift z . The collapse threshold does not depend on any intrinsic property of the halo, but rather on the shape and strength of the surrounding tidal field, i.e. on e and p . In the left-hand panel of Fig. 1 we plot the overdensities of protohaloes, δ_h , linearly extrapolated to z_{id} , as a function of the tidal field ellipticity, e . Both quantities have been averaged over a spheri-

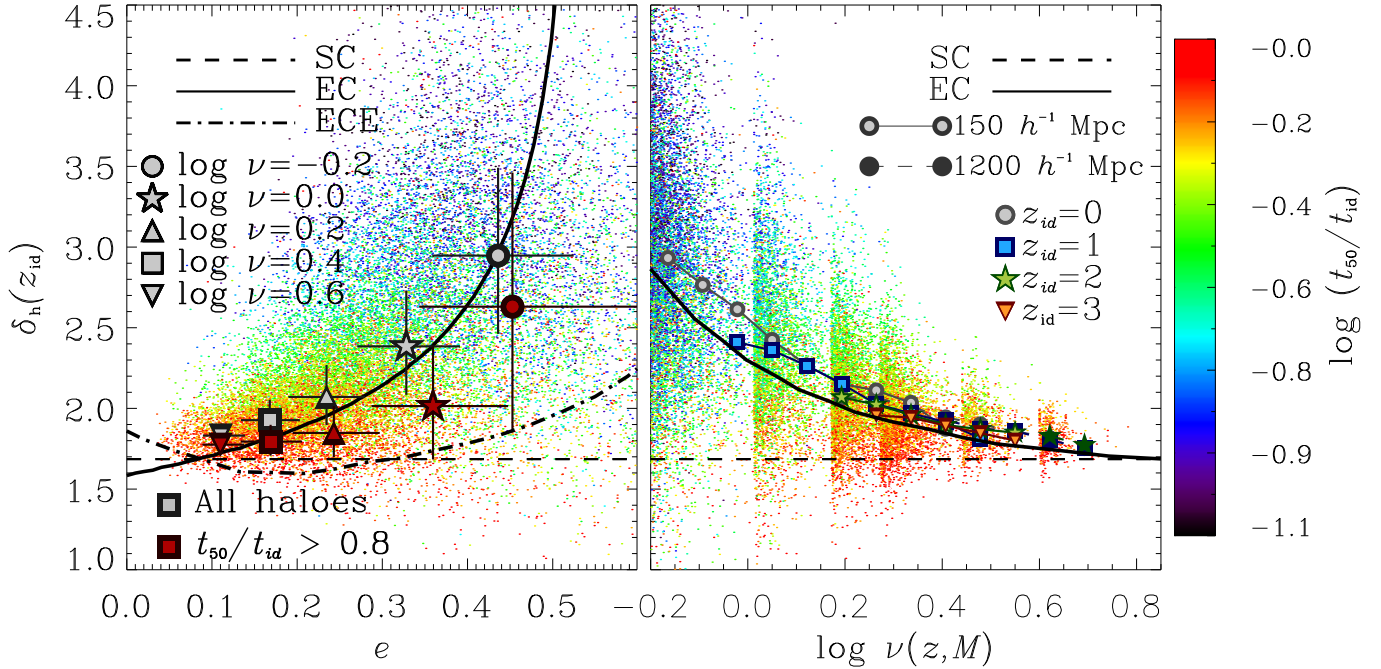


Figure 1. Lagrangian overdensities of protohaloes linearly extrapolated to their identification redshifts, $\delta_h(z_{id})$, plotted as a function of the ellipticity of the surrounding tidal field (left) and the dimensionless “peak height” mass parameter, $\nu(z, M) = \delta_{sc}(z)/\sigma(z, M)$ (right). Light (grey) symbols with error bars in the left-hand panel plot the median δ_h and e for haloes that fall in narrow bins of peak height centred on the value indicated in the legend; error bars indicate the 25th and 75th percentiles of the scatter. Darker (red) symbols correspond to the medians and scatter for the subsample of haloes in each ν bin that have $t_{50}/t_{id} > 0.8$, corresponding to recently collapsed systems. The heavy solid curve shows the predictions of the EC model of BM96; the dashed curve corresponds to the collapse threshold for an initially triaxial perturbation with axis ratios consistent with those of M_* haloes: $q_2/q_1 = 0.75$ and $q_3/q_1 = 0.55$ (for simplicity, both models assume a prolaticity $p = 0$). In the right-hand panel, the same overdensities are plotted as a function of peak height, ν . Heavy connected points trace the median relation for haloes identified at different redshifts, z_{id} . The good agreement at overlapping ν indicates that our results are not unduly influenced by numerical artefacts. The thick solid line in the right-hand panel shows the predicted mass dependence of the BM96 EC model assuming that $e = (\sigma/\delta)/\sqrt{5}$ (e.g. Sheth et al. 2001). In both panels, the horizontal dashed line shows the SC barrier, $\delta_{sc} = 1.686$.

cal Lagrangian volume enclosing the halo mass¹. Individual points correspond to haloes (with $N_{\text{FOF}} \geq 500$) identified at each of the four redshifts mentioned above. The heavy, light-colored symbols plot the median values of δ_h and e in several narrow bins of the dimensionless peak height parameter², $\nu(z, M) = \delta_{sc}(z)/\sigma(z, M)$, as indicated in the legend; the horizontal and vertical error bars highlight the 25th and 75th percentiles of the scatter along each axis. (We have verified that, within the statistical error, the median values of δ_h and e at each ν are independent of z_{id} .)

Note that these points follow very closely the thick solid line, which corresponds to the collapse threshold predicted by the EC model of BM96 (assuming $p = 0$, the most probable value for random points in a Gaussian random field). The agreement between the simulations and the EC model

is quite remarkable given its simplicity. This supports the model’s theoretical underpinning, in which more strongly sheared perturbations – typically those with larger ellipticities, e – require higher initial overdensities to collapse at z_{id} .

Never the less, at any ν , the scatter in both δ_h and e is large, and correlates strongly with the characteristic formation time of each halo. This can be seen in the colour coding of points, which highlight gradients in the formation time variable $\log(t_{50}/t_{id})$, as indicated in the colour bar on the right. This scatter, and its dependence on z_{50} , cannot be accounted for by halo-to-halo variation in tidal prolaticity alone (see, e.g., Hahn & Paranjape 2014) suggesting that other factors are at play.

Note that the solid curve in Fig. 1 was constructed for $p = 0$ and assumes $z_c = z_{id}$; it therefore represents a lower limit to the collapse threshold (for collapse at $z_c > z_{id}$, the density threshold would be larger by a factor $D(z_{id})/D(z_c)$). If in reality $z_c = z_{id}$, and all haloes are collapsing just at the moment they are identified, then their linear overdensities would trace the true underlying barrier. Intriguingly, the vast majority of *recently collapsed haloes* lie below the ellipsoidal collapse threshold. Instead, these haloes sit slightly above the spherical threshold, $\delta_{sc} = 1.686$, shown as

¹ We have verified that, for protohaloes with >500 particles, discreteness effects in our linear density field do not influence our estimates of δ_h and e are negligible (see Hahn & Paranjape (2014) for an alternative method for measuring these quantities.)

² The choice of peak height, ν , is more natural than mass when comparing haloes across different redshifts. It describes halo masses relative to the characteristic halo mass, M_* , at z_{id} , defined by $\nu(M_*, z_{id}) = 1$.

a dashed line in this plot. This is clearly at odds with the expectations of the EC model, which predicts that haloes with $z_c \approx z_{id}$ should trace the solid curve, and those with $z_c > z_{id}$ to scatter to higher δ_h . The heavy (red) filled symbols in the left-hand panel make this point clear. These show the median values of δ_h and e (in narrow bins of ν , centred on the values indicated in the legend) but for haloes with $t_{50}/t_{id} > 0.8$, corresponding to recently collapsed systems. Although the tendency of δ_h to increase with e remains, the dependence is much weaker than predicted by standard ellipsoidal dynamics: these points fall systematically below the solid curve. More important for EPS theory is the mass dependence of the collapse threshold. We can use the linear overdensities of our haloes, extrapolated to the halo identification epoch, to relate δ_h to the halo's final mass at z_{id} (or equivalently, its fluctuation amplitude). We show this in the right hand panel of Fig. 1. The thick solid curve shows the ellipsoidal collapse threshold predicted by the model of BM96, mapped on to halo mass using the most probable $e - \sigma(M)$ relation for random points in a Gaussian random field: $e = (\sigma/\delta)/\sqrt{5}$ (Doroshkevich 1970; Sheth et al. 2001).

In agreement with previous work (Dalal et al. 2008; Robertson et al. 2009; Elia et al. 2012), we find that the measured protohalo overdensities decrease with halo mass in a manner that resembles the predictions of the EC model. The agreement, however, is not perfect: at any given mass scale, the median Lagrangian overdensity of protohaloes slightly exceeds δ_{ec} . More importantly, we find that, for the most recently collapsed systems, the mass dependence of δ_h is much weaker than expected from the ellipsoidal model, even though it is precisely these systems that we expect to follow the true threshold for collapse at z_{id} .

3.2 Shapes

The standard EC model is based on the assumption that protohalo geometries are perfectly spherical; during collapse, the surrounding tidal field distorts the sphere into an ellipsoid and evokes the notion of “ellipsoidal” collapse. However, as noted by Porciani et al. (2002), Lagrangian regions that collapse to form DM haloes by $z = 0$ are manifestly non-spherical (see also Ludlow & Porciani 2011; Despali et al. 2013). In the EC model, initially triaxial perturbations will affect the dynamics of collapse, since the initial displacement of the outermost shell (more precisely, the boundary of the perturbation) differs along each of the three principal axes of the ellipsoid. This inevitably alters the collapse time of each axis and, as a result, the overdensity required for complete collapse to occur by a particular time.

In Fig. 2 we plot the mass dependence (expressed as a function of ν) of the initial axis ratios, q_2/q_1 and q_3/q_1 , of protohaloes in both of our simulations. Coloured points show separately the median trends for the Lagrangian progenitors of haloes identified at each z_{id} ; and full or outlined points distinguish those identified in our 1200 and 150 h^{-1} Mpc boxes, respectively. Thin solid (150 h^{-1} Mpc) and dashed (1200 h^{-1} Mpc) lines in both panels indicate the first and third quartiles in each ν bin (shown only for the $z_{id} = 0$ sample, for clarity). The good agreement between the median trends and scatter at overlapping mass scales suggests that our shape estimates are not unduly affected by resolution.

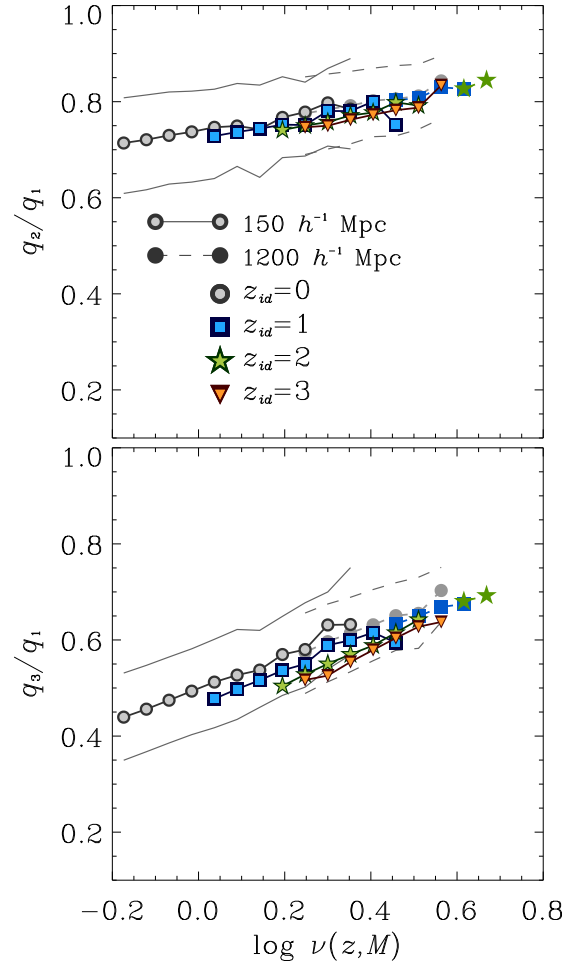


Figure 2. Axis ratios, q_2/q_1 (top) and q_3/q_1 (bottom), of protohaloes in the initial conditions of our simulations as a function of peak height, ν . Connected points show the median trends, with different symbols used to distinguish protohaloes according to the redshift at which their descendants were identified, z_{id} . Outlined points connected by solid lines show results for protohaloes in our 150 h^{-1} Mpc box; solid points for those in our 1200 h^{-1} Mpc box. For $z_{id} = 0$, the first and third quartiles of the scatter are indicated using thin solid (150 h^{-1} Mpc box) or dashed (1200 h^{-1} Mpc) lines.

When expressed in term of peak height, ν , protohalo shapes are largely independent of the redshift at which their descendants are identified. This suggests that, on average, the rarity of the peak, or equivalently its fluctuation amplitude, determines the geometry of the collapsed region (see also Despali et al. 2014). This is not true for individual haloes, however, and we discuss this point further in Section 3.4.

More importantly, we find that protohalo shapes depend weakly but systematically on ν , with rarer fluctuations becoming increasingly more spherical. We can quantify the departure from spherical symmetry by the “sphericity”, q_3/q_1 , which varies, on average, from ~ 0.42 for haloes with $\nu \approx 0.6$ to ~ 0.65 for the protohaloes of the rarest, most massive haloes at z_{id} . Note also that spherical protohaloes are quite rare. Fewer than ~ 0.3 per cent of haloes with

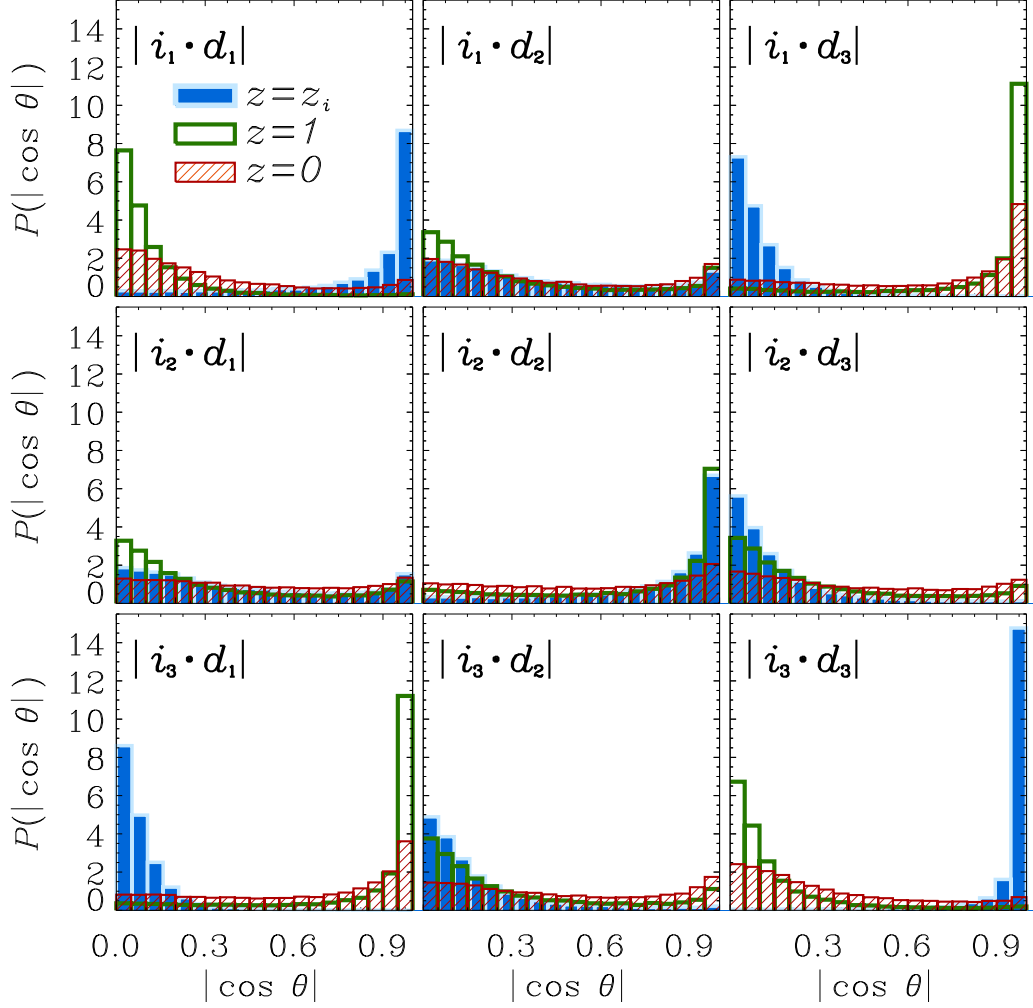


Figure 3. Alignment of the principal axes of the inertia, I_{ij} , and deformation, \mathcal{D}_{ij} tensors for haloes and protohaloes in our $150 h^{-1}$ Mpc box. Only haloes in the ($z_{\text{id}} = 0$) mass range $24.3 < M_{\text{FoF}}/(10^{10} h^{-1} \text{M}_{\odot}) < 48.7$ are included. Blue shaded histograms are used for protohaloes in the initial conditions of the simulation; open (green) and (red) hatched histograms show the alignments measured at $z = 1$ and 0 , respectively. The eigenvalues are ordered such that $j = 1$ corresponds to the major axis and $j = 3$ to the minor. The initial alignment between the principal axis frames of the inertia and tidal tensors changes as the system collapses, reflecting changes in the ordering of the eigenvectors of the inertia tensor.

$\nu \approx 0.6$ have $q_3/q_1 \geq 0.8$. This fraction increases to ~ 0.5 per cent for $\nu \approx 1$, and to ~ 6.6 per cent for $\nu \gtrsim 3$.

3.3 Orientation

The orientation of the principal axis frames of protohaloes is closely related to the external tidal field acting upon them (Porciani et al. 2002, see also Lee & Pen, 2000). This connection is illustrated in Fig. 3, where we plot the distribution of angles between the three principal eigenvectors of the inertia, \mathbf{i}_i , and shear tensors, \mathbf{d}_i , for protohaloes in the ($z_{\text{id}} = 0$) mass range $24.3 < M_{\text{FoF}}/(10^{10} h^{-1} \text{M}_{\odot}) < 48.7$. The different histograms correspond to different times at which the alignment was measured: filled (blue) histograms show the alignment measured at z_i , the initial redshift of our simulations; the open (green) histograms correspond to $z = 1$, and the hatched (red) histograms to the final output, at $z = 0$.

Note that, at all times, we track the same set of haloes, and include all particles associated with each at $z = 0$ in the calculation of the inertia tensor.

At z_i , the peak near $|\cos \theta| \approx 1$ in the diagonal panels indicates that the long, intermediate and short axes of the principal axis frames of \mathcal{D} and I share the same orientation (see also Porciani et al. 2002; Despali et al. 2013). The upper-right and lower-left panels also show that the minor axis of either tensor lies orthogonal to the major axis of the other. The alignment is such that the direction of maximum compression coincides with the major axis of the protohalo, whereas its minor axis coincides with the axis of weakest compression, or dilation. This coincidence in orientation is actually *expected* if the shape of the tidal field dictates the Lagrangian region from which particles can accrete by a given time.

At later times the alignment shifts. At $z = 1$, for ex-

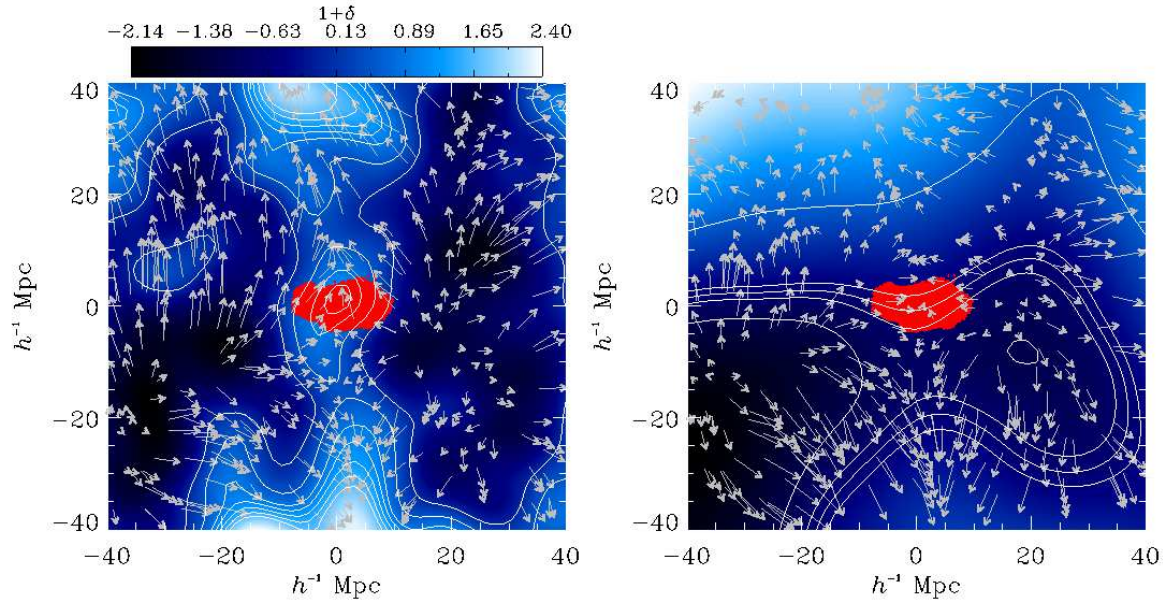


Figure 4. Linear over-density (left) and peculiar gravitational potential (right) fields in the vicinity of a $\sim 3 \times 10^{13} h^{-1} M_{\odot}$ protohalo identified in our $150 h^{-1}$ Mpc box simulation. The protohalo is shown using red dots; thin white lines highlight contours of fixed over-density and potential that have been over-laid to guide the eye. Both fields have been smoothed on the halo mass scale and linearly extrapolated to $z = 0$. The halo forms in the vicinity of a density peak with the same characteristic mass, but has a markedly different shape and orientation. This is because the geometry of the peak is determined by a density threshold, whereas the protohalo shape and orientation are determined by the external tidal field generated by the surrounding large-scale structure. The flow of DM on to and around the protohalo is shown using thin arrows. In the left-hand panel these arrows mark the total bulk velocity field, whereas those on the right show the flow in the halo rest frame.

ample, the shortest axis of the ellipsoid typically aligns with \mathbf{d}_1 , and the longest axis with \mathbf{d}_3 . This change in orientation is at odds with the collapse dynamics envisioned by the BM96 EC model, in which the alignment remains fixed at all times. However, as we will see below, the ordering of the principal axes of I may change during collapse if the initial perturbation is non-spherical yet perfectly aligned with the principal axes of the deformation tensor: the apparent change in orientation reflects a change in the ordering of the principal axes frame of the protohalo as it collapses. Two axes switch their order instantaneously at the moment in which they have equal lengths. In reality, however, there will always be a small degree of misalignment between the inertia and shear tensors which will cause a continuous deformation of the protohalo until \mathbf{i}_1 and \mathbf{i}_3 align with \mathbf{d}_3 and \mathbf{d}_1 , respectively (Despali et al. 2013). This initial misalignment will also generate a small net angular momentum in the collapsing ellipsoid. Finally, note that the alignment is still evident at $z = 0$, but less so. This is a result of the more spherical geometry of virialized systems, and the fact that internal shear (generated by the non-spherical halo shape itself) dominates the tidal field due to the halo’s high density contrast.

3.4 Relationship between shape, shear and orientation

If boundaries of protohaloes are determined by the external tidal field then both the relative magnitude and sign of the eigenvalues, λ_i , establish their over-all shape. In

Fig. 4 we show an example of this, where we plot the linearly extrapolated density field, $1 + \delta$, centred on a $\sim 3 \times 10^{13} h^{-1} M_{\odot}$ protohalo (red dots) in the initial conditions of our $150 h^{-1}$ Mpc box simulation. The contours enclosing the density peak around which the halo collapses provide an intuitive picture of the spatial distribution of DM in its vicinity: its mass distribution is extended along a high-density ridge connecting two massive structures and separating two low-density voids. The long axis of the *protohalo*, however, lies transverse to that of the density peak, and it is easy to understand why. Material flows out of the voids towards the higher density filament along an axis roughly perpendicular to it, whereas the large-scale overdensities result in dilation along the ridge. The net effect is a push-and-pull of material that sets the shape and orientation of the protohalo such that its long axis coincides with the direction of maximum compression, or infall, and its short axis to the direction of maximum expansion. The grey arrows in Fig. 4 sample the linear velocity field and help clarify the impact of large-scale tides on gravitational collapse around the density peak.

The fact that the mass distribution associated with the density peak differs substantially from that of the protohalo indicates that the tidal forces associated with the surrounding large-scale structure dominate over the internal shear generated by the peak’s mass distribution. In the right-hand panel of Fig. 4 we show the smoothed potential field in the same region. Thin white lines show iso-potential contours and arrows the velocity field measured in the halo rest frame. Clearly the largest potential gradient lies along the shortest axis of the protohalo, with the long axis roughly bounded by iso-potential contours. The shapes of protohaloes are thus

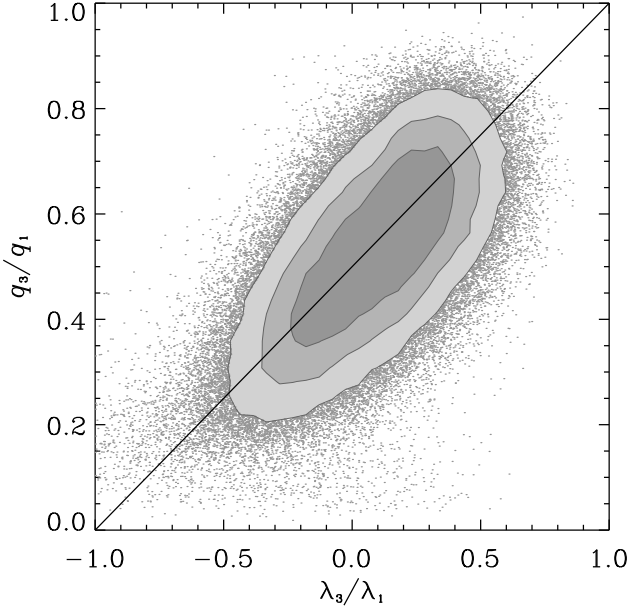


Figure 5. Minor-to-major axis ratios, q_3/q_1 , of protohaloes versus the ratio λ_3/λ_1 of the tidal deformation tensor measured at their centres of mass. Contours enclose 50, 75 and 90 per cent of the data, with the remaining 10 per cent shown using grey dots. For clarity, we only plot haloes identified at $z_{\text{id}} = 0$ that also contain more than 500 particles.

determined by asymmetry in the large-scale tidal field rather than by the shapes of the peaks from which they form.

In Fig. 5 we plot the ratio q_3/q_1 versus λ_3/λ_1 for all protohaloes (corresponding to DM haloes identified at $z_{\text{id}} = 0$) in our simulations (that contain at least 500 particles). The filled contours enclose 50, 75 and 90 per cent of the data, with the remaining haloes shown individually as dots. The strong correlation between the protohalo sphericity and the asymmetry of surrounding tidal field can be understood as follows. The limiting spherical case, in which all λ_i s are equal, corresponds to an isotropic tidal field. In this case there is no preferred orientation of the tidal forces acting upon linear perturbations and collapse occurs roughly isotropically, resulting in $q_3/q_1 \approx q_2/q_1 \approx 1$. A decrease in λ_3/λ_1 , however, corresponds to larger dilation along the minor axis of the tidal field, \mathbf{d}_3 , relative to the enhanced compression along \mathbf{d}_1 . This drives material away from the perturbation along \mathbf{d}_3 while boosting accretion along \mathbf{d}_1 . This results in a more flattened geometry (i.e., lower values of q_3/q_1) as material from larger initial displacements can reach the centre along \mathbf{d}_1 in a given time. As we will see in the next section, these correlations have important implications for collapse thresholds inferred from the EC model.

These results cast doubt on the validity of previous work in which the Lagrangian volumes of protohaloes are assumed to coincide with isodensity contours drawn around local maxima in the linear density field. The density distribution in the vicinity of a peak located at \mathbf{x}_p can be approximated by a Taylor expansion about the peak:

$$\delta(\mathbf{x}_p) \simeq \delta_0 - \frac{1}{2} \frac{\partial^2 \delta}{\partial x_i \partial x_j} (x - x_p)_i (x - x_p)_j + \dots, \quad (6)$$

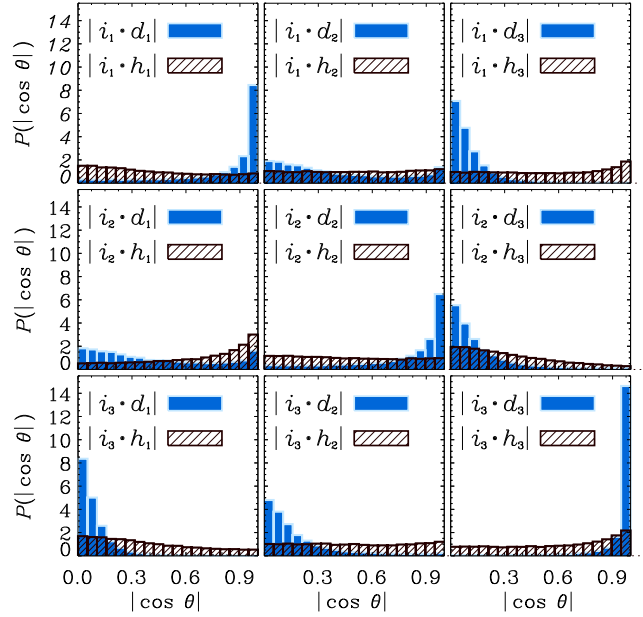


Figure 6. Alignment of principal axes of the protohalo inertia tensor, I_{ij} , with those of the tidal field (filled blue histograms) and of the Hessian of the overdensity field (black hatched histograms). The latter quantities are measured at protohalo centres of mass and have been averaged over a spherical Lagrangian region containing the halo mass. As in Fig. 3, only haloes in the ($z_{\text{id}} = 0$) mass range $24.3 < M_{\text{FoF}}/(10^{10} h^{-1} M_{\odot}) < 48.7$ are included and, in all cases, the eigenvalues are ordered such that $j = 1$ corresponds to the major axis and $j = 3$ to the minor axis. As anticipated, the peak shapes are oriented randomly with respect to the protohalo mass.

where $\partial_i \partial_j \delta$ is the Hessian matrix of the density field. This matrix can be diagonalized; its eigenvalues and eigenvectors, denoted \mathbf{h}_i , describe the shape and orientation of the peak, respectively. Heavens & Peacock (1988) used this description of the peak's mass distribution to estimate the total mass associated with a given density maxima, while Catelan & Theuns (1996) used the misalignment between the eigenvectors of the peak and those of the surrounding tidal field to calculate the growth of angular momentum in proto-galactic haloes.

We explore the validity of this assumption in Fig. 6, where we plot, using black hatched histograms, the distribution of angles between the principal axis frames of the protohalo inertia tensor and those of the density Hessian at the protohalo location. Only ($z_{\text{id}} = 0$) haloes in the mass range $24.3 < M_{\text{FoF}}/(10^{10} h^{-1} M_{\odot}) < 48.7$ are included. For comparison, we also show the alignment between the eigenvalues of I_{ij} and of D_{ij} (blue filled histograms). These results indicate that protohaloes are essentially randomly oriented with respect to the underlying matter distribution, which strengthens our conclusion that the large-scale tidal field ultimately dictates the shape and orientation of protohalo regions.

4 THRESHOLDS FROM ELLIPSOIDAL COLLAPSE

In order to better understand these results we here critically examine the EC model, bearing in mind the findings presented above. In particular, we describe a general model for homogeneous ellipsoidal collapse that follows the evolution of an *initially triaxial* overdensity in the presence of an evolving external tidal field. We will refer to this model as ECE (for Ellipsoidal Collapse of Ellipsoidal perturbations) in order to distinguish it from the standard EC model. We will use it to study the impact of protohalo shapes on collapse thresholds inferred from ellipsoidal collapse dynamics. The dynamical equations for the ellipsoid are derived in full detail in Appendix A.

4.1 Homogeneous Ellipsoidal Collapse

We consider a uniform density perturbation in an otherwise unperturbed Friedmann–Robertson–Walker background whose energy content is dominated by the matter density, ρ_m , and a cosmological constant, Λ . We model the perturbation as a homogeneous ellipsoid with semi-axes of physical length r_i ($i = 1, 2, 3$) and density contrast, δ . We adopt a Cartesian coordinate system, x_i , that aligns with the principal axes of the ellipsoid, as well as with the external tidal field (see Fig. 3).

In this coordinate system, the axis lengths of the Lagrangian ellipsoid, r_i , will obey the following equation of motion:

$$\frac{\ddot{r}_i}{r_i} = \frac{\Lambda c^2}{3} - 4\pi G \rho_m \left(\frac{1+\delta}{3} + \frac{\beta_i}{2} \delta + \lambda_i^{\text{ext}} \right). \quad (7)$$

Here c is the speed of light and λ_i^{ext} is the i th eigenvalue of the *external* tidal field. The β_i characterizes the internal shear generated by the shape of the perturbation and can be calculated using standard elliptic integrals (e.g., equation A2 in the Appendix).

Once the initial external tidal field has been specified, solving equation (7) requires a prescription for its subsequent time evolution. We assume that external tides are dominated by large-scale structure and approximate their evolution according to linear theory, i.e. $\lambda_i^{\text{ext}}(t) \propto \lambda_{i,0}^{\text{ext}} D(t)$. The internal tides associated with the evolving perturbation are calculated self-consistently within the model and depend, at any moment, on its overdensity and shape.

Because the potential is quadratic and the acceleration is linear in the coordinates, concentric ellipsoids with the same axis ratios evolve self-similarly; the perturbation therefore remains homogeneous at all times and satisfies

$$1 + \delta = \frac{q_1 q_2 q_3}{r_1 r_2 r_3} (1 + z)^{-3}, \quad (8)$$

where the q_i s denote the *initial* comoving principal axis lengths of the ellipsoid. The density contrast grows with time, diverging when any one axis fully collapses. In reality, however, small initial departures from perfect symmetry are enhanced during collapse, and result in a stable structure close to virial equilibrium (BM96). We approximate this virialization process by halting collapse along each of the three axes once they reach a fraction f of their initial comoving radius. Note that the value of f has no fundamental physical meaning, but $f = 0.178$ reproduces the virial

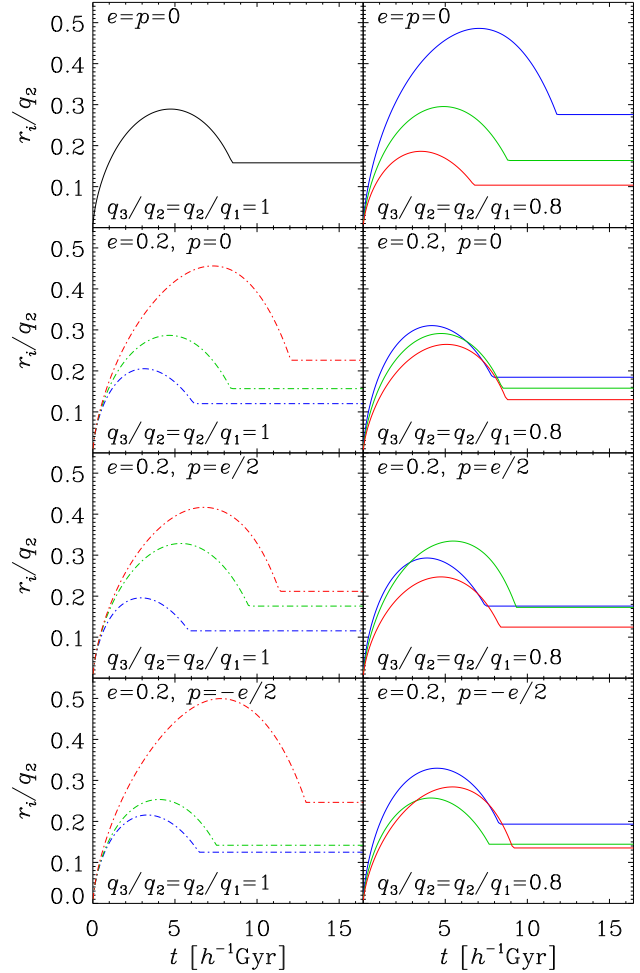


Figure 7. Evolution of the axis lengths for collapsing ellipsoids, expressed in units of the initial intermediate axis length, q_2 . Left-hand panels assume that the initial overdensity is a uniform sphere, as in the model of BM96; right-hand panels adopt an initially triaxial overdensity with axis ratios $q_2/q_1 = q_3/q_2 = 0.8$. Top panels assume negligible tidal forces. Lower panels have a (total) tidal field ellipticity of $e = 0.2$, and show results for three different prolativities, $p = 0$ (the characteristic value for random points in a Gaussian random field), as well as $p = e/2$ and $p = -e/2$, as indicated in the legends. In each case, the quoted e and p correspond to the *total* tidal field. Note that relaxing the assumption of spherical symmetry substantially changes the collapse times of each axis. Axes are color-coded according to their alignment with the initial tidal field: blue curves align with \mathbf{d}_1 , green with \mathbf{d}_2 and red with \mathbf{d}_3 .

overdensity of ~ 178 for spherical collapse in an Einstein–de Sitter universe. For simplicity, we will also adopt $f = 0.178$ in our EC model, but note that the final overdensities of haloes in this case will differ depending on the details of collapse.

In Fig. 7 we plot the trajectories of the three axes lengths, in physical units, for the EC model of BM96 (left-hand panels) and for the modified ECE model described above (right). We start our numerical calculations at $t_0 = 0.250$ Myr and assume, in each case, the same initial density contrast. The top two panels show the evolution of an ini-

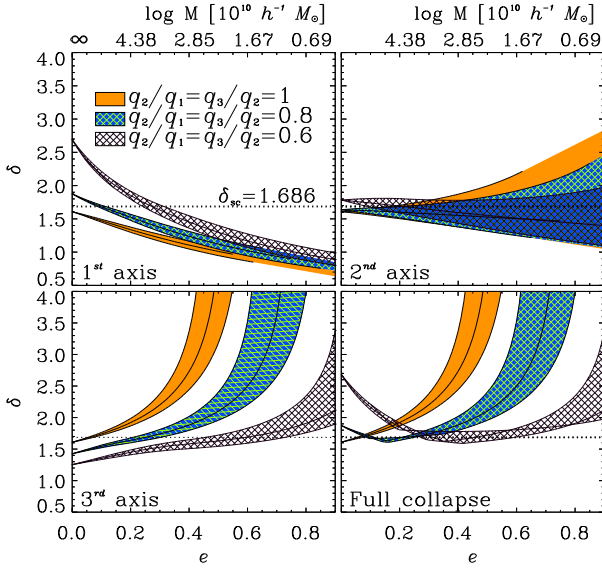


Figure 8. Comparison of the collapse boundaries predicted by the EC model for three initial perturbation shapes. The different panels show separately the linearly extrapolated over-density required for collapse to occur along the primary axis (top-left), the intermediate axis (top-right) and the minor axis (bottom-left) of the initial perturbation. The bottom-right panel shows the barrier height required for all three axes to collapse by the present day. The shaded and hatched regions demonstrate the effect of varying the prolaticity of the tidal field over the range $-e/2 \leq p \leq e/2$. Orange, blue and white regions show results for three initial shapes: $a_2/a_1 = a_3/a_2 = 1$, $a_2/a_1 = a_3/a_2 = 0.8$, and $a_2/a_1 = a_3/a_2 = 0.6$, respectively. In all cases, the major axis of the tidal field is assumed to be aligned with the major axis of the initial perturbation; the corresponding intermediate and minor axes are also aligned.

tially spherical (left) and ellipsoidal perturbation with axis lengths $a_2/a_1 = a_3/a_2 = 0.8$ (right) when no external tides are present. The lower panels show, for the same initial setup, the effect of varying the external tidal field on the evolution of the axis lengths.

Notice how relaxing the assumption of spherical symmetry at t_0 changes substantially the evolution of the axis lengths, even when the tidal field is chosen to be identical. In particular, the ordering of the principal axes change with time; what is initially the primary axis, for example, can swap between intermediate and minor, and then back to primary again. This explains the time-dependence of the alignment between the principal axes of the inertia and shear tensors seen in Fig. 3. Note that this reordering of the principal axes i_i is impossible to achieve when linear perturbations are assumed to be spherical; in this case their orientation at all $t > t_0$ depends entirely on the shape of the initial external tidal field.

In addition, note that the turnaround and freeze-out times also differ for initially triaxial perturbations. As shown in Fig. 8, this has important implications for modelling collapse boundaries for halo formation. In each panel, orange, blue and white-hatched regions show the collapse thresholds for perturbations with initial axis ratios $q_2/q_1 = q_3/q_2 = 1$,

0.8 and 0.6, respectively. Thick solid lines show results for $p = 0$; the shading and hatching demonstrates the effect of varying the tidal prolaticity over the range $-e/2 \leq p \leq e/2$. Each panel plots separately the linearly extrapolated density contrast required for collapse to occur today along one of the three principal axes of the initial perturbation. (The first axis corresponds to what is initially the major axis of inertia; the third to the minor axis.)

For a given e and p , collapse along the major axis of an initially non-spherical perturbation always requires a higher linear density contrast than for an initial sphere. This is because the internal shear generated by an ellipsoidal perturbation always suppresses collapse along the perturbation's major axis, which is, additionally, located at a larger initial displacement than in the spherical case. Along the minor axis of the initial ellipsoid, however, collapse thresholds are always lower than in the spherical case. This is because the internal shear acting along this axis always aids in collapse, and large values of tidal ellipticity (corresponding to large and negative values of λ_3) are required to counteract this.

The lower right panel of Fig. 8 shows the ellipsoidal threshold, B_{ec} , required for all three perturbation axes to collapse at $z_c = 0$. Clearly, even modest changes in initial shape of the perturbation affects the inferred barrier considerably. For example, the heavy dot-dashed line in the left panel of Fig. 1 shows B_{ec} computed for a perturbation with axis ratios $q_2/q_1 = 0.75$ and $q_3/q_1 = 0.55$, approximately equal to the mean values for haloes with masses $\sim M_*$. Now essentially *all* haloes lie *above* the *ellipsoidal collapse barrier*, which provides an accurate *lower bound* the typical overdensities of recently collapsed systems.

4.2 Shape dependence of barrier heights

With estimates of the shapes, overdensities and tidal ellipticities of protohaloes, we can test the shape dependence of barrier heights predicted by the ECE model discussed above. The distribution of protohaloes in the (δ_h, e) plane is shown in Fig. 9 for objects in three bins of initial shape. For simplicity, we only consider haloes with $\nu \approx 1$ but note that our conclusions hold for other halo masses and at all redshifts. From left to right, panels correspond to protohaloes with increasing triaxiality. The left-hand panel plots approximately spherical protohaloes, selected to have $q_3/q_1 > 0.8$. The middle and right-hand panels show triaxial systems whose axis ratios (q_2/q_1 and q_3/q_2) fall in the ranges 0.65 to 0.75, and 0.45 to 0.55, respectively. As in Fig. 1, we have coloured points according to the logarithm of the half-mass formation time measured relative to the age of the Universe at z_{id} : $\log(t_{50}/t_{id})$.

As discussed in the previous section, protohalo shapes have a significant effect on the density contrast required for collapse. Compared to their spherical counterparts, non-spherical protohaloes require higher density contrasts to collapse when no tidal fields are present, but collapse at lower density contrasts in the presence of strong external tides. They exhibit a range of tidal ellipticities over which $\delta_{ec} \approx \delta_{sc} = 1.686$ that broadens with increasing (initial) departure from sphericity. This explains why the triaxial protohaloes in Fig. 9 tend to move to higher values of e , but not to higher δ_h , as expected from the standard EC model.

The solid curves in each panel of Fig. 9, for example,

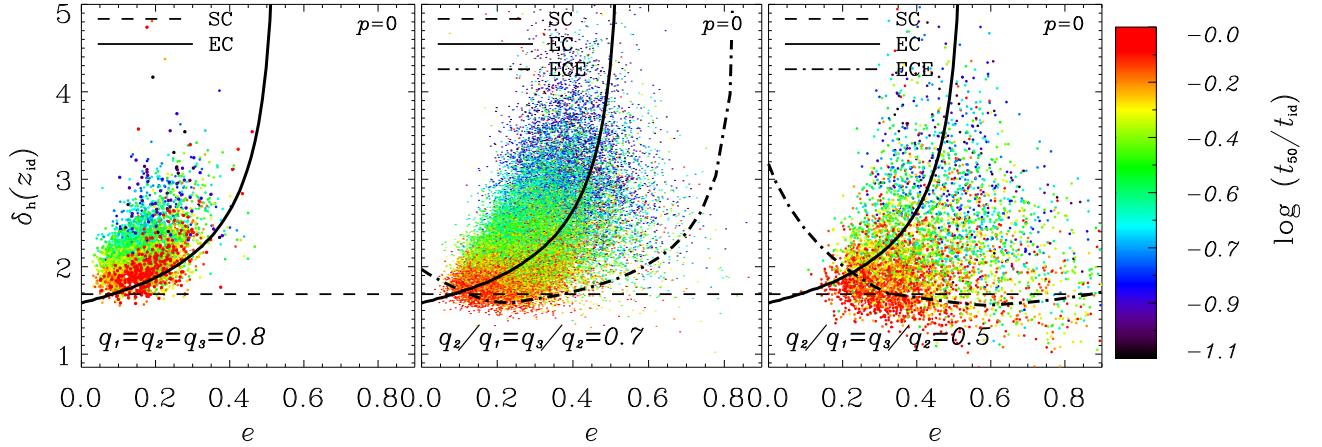


Figure 9. Linear overdensities of protohaloes, $\delta_h(z_{id})$, as a function of the ellipticity of the surrounding tidal field, e , for haloes in three separate shape bins. Left-hand panels show “spherical” protohaloes, with $q_3/q_1 > 0.8$; middle and right-hand panels show subsamples with axis ratios q_2/q_1 and q_3/q_2 that fall in the range (0.65, 0.75) and (0.45, 0.55), respectively. All points have been colour-coded by the formation time variable $\log(t_{50}/t_{id})$, according to the colour-bar on the right. The solid line in each panel shows the collapse threshold predicted by the classic EC model described by BM96, which assume an initially spherical perturbation geometry. The dot-dashed lines show the model predictions assuming initial perturbation shapes of $q_2/q_1 = q_3/q_2 = 0.7$ (middle) and 0.5 (right) (referred to as the ECE model). Horizontal dashed lines show the SC threshold, $\delta_{sc} = 1.686$. Note that the ellipsoidal collapse threshold obtained for spherical perturbations provides a poor description of the distribution of the linear overdensities of non-spherical systems, particularly for the most recently collapsed ones (shown using red colours on this colour-scale).

shows the ellipsoidal collapse threshold for initially spherical protohaloes (for $p = 0$), which provides a good description of the minimum overdensities of spherical systems (left-most panel), particularly those with recent formation times (red points). Note however, that this curve describes rather poorly the measured overdensities of the non-spherical protohaloes shown in the other two panels. Never the less, when the initial shapes of protohaloes are included in the calculation of B_{ec} , the ellipsoidal model again provides a good description of their minimum Lagrangian overdensities. The dot-dashed curves in Fig. 9 show B_{ec} computed for protohaloes with $q_2/q_1 = q_3/q_2 = 0.7$ (middle panel) and 0.5 (right-hand panel), which trace rather well the minimum locus of points in each panel. Finally, note that, in all shape bins, the most recently collapsed haloes (shown as red points on this colour scale) neatly trace the ellipsoidal collapse barrier provided their initial shapes have been properly modelled.

These results imply that the standard model for ellipsoidal collapse outlined by BM96 provides a poor description of the Lagrangian overdensities of non-spherical protohaloes. We quantify this further in Fig. 10, where we plot the fraction of haloes for which $\delta_h(z_{id}) \geq \delta_{ec}$ as a function of the minor-to-major axis ratio of the protohalo. For clarity, we only consider protohaloes of $z_{id} = 0$ haloes, but show results for objects in three separate bins of peak height: $\nu \approx 1, 2$ and 2.5. In the upper panels we plot the distribution of q_3/q_1 for each ν bin. Note that B_{ec} has been computed individually for each halo using their measured e and p , assuming either a spherical protohalo geometry (solid lines), or using the protohalo’s measured initial shape (dot-dashed lines).

Assuming spherical symmetry when calculating δ_{ec} , the fraction of protohaloes that fall below the predicted collapse threshold depends sensitively on their initial shapes. Only those with initially spherical geometries are denser than the

EC threshold given the initial strength of their surrounding tidal field. This is perhaps not surprising given that this model *assumes* initially spherical perturbations. Below $a_3/a_1 \sim 0.7$ the fraction of haloes with $\delta_h > \delta_{ec}$ drops dramatically; only $\sim 40\%$ of those with $a_3/a_1 \sim 0.4$ satisfy this restriction. However, when their initial shapes have been included in the calculation of the collapse threshold virtually all protohaloes have $\delta_h > B_{ec}$. Protohalo shapes are therefore an important ingredient in analytic models that attempt to relate regions of the Lagrangian density field to the statistics of Eulerian haloes at later times. Note also that both trends are approximately independent of halo mass: the three bins of peak height used in Fig. 10 span nearly two orders of magnitude in halo mass.

5 DISCUSSION

The average linear overdensity of DM protohaloes increases with tidal-field strength in a way that resembles the predictions of the EC model of BM96 (see also, Dalal et al. 2008; Robertson et al. 2009; Elia et al. 2012). By following the collapse of individual protohaloes, and matching them to non-linear objects identified at later redshifts z_{id} , we have shown that the scatter in $\delta_h(z_{id})$ correlates strongly with the halo’s “formation time”, z_{50} , at which half of its final mass was first assembled into one progenitor. Intriguingly, our results indicate that most recently formed haloes do not trace the classic ellipsoidal collapse barrier but fall systematically below it.

By modifying the classic EC model to follow the collapse of an initially triaxial perturbation (rather than a spherical one) one can approximately capture the *minimum* overdensities of protohaloes as a function of e . However, in this case a conceptual problem arises from the fact that our model

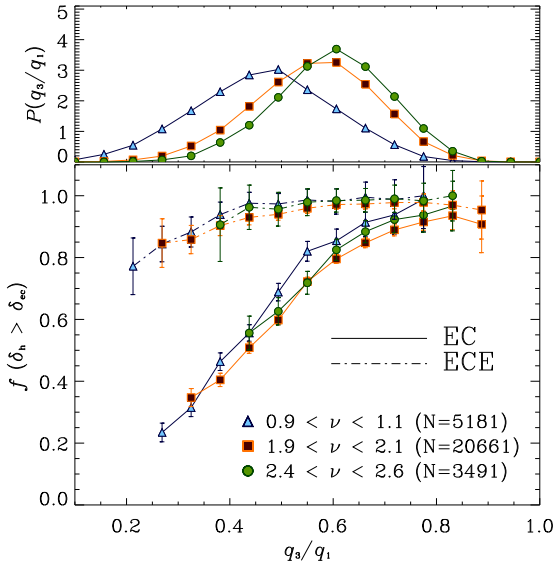


Figure 10. Fraction of protohaloes as a function of “sphericity” (q_3/q_1) with linear density contrasts that exceed the ellipsoidal collapse threshold, δ_{ec} . Different symbols correspond to different masses, characterized here using the peak-height mass parameter, ν (note that we only consider protohaloes of $z_{id} = 0$ systems here). Different line styles are used to distinguish collapse thresholds computed for initially spherical perturbations (solid) from those that use the measured protohalo shapes (dot-dashed lines).

predicts rather well the minimum overdensities of collapsed regions, rather than the mean as is the case for the BM96 model. In EPS or peaks theory, one assumes that a given mass element at \mathbf{x} will be associated with a halo of mass M at redshift z_{id} provided its overdensity, smoothed with a filter of mass M and linearly extrapolated to that redshift, has the value $\delta_M(\mathbf{x}, z_{id}) \equiv B(z_{id})$. Why, then, do haloes with $\delta_h(z_{id}) > B$ exist when there is certainly a larger mass scale $M' > M$ for which $\delta_{M'}(\mathbf{x}, z_{id}) \equiv B(z_{id})$ is satisfied?

One possibility is that evolutionary effects truncate mass accretion on to haloes at redshifts $z > z_{id}$. This is possible, for example, if haloes were previously associated with and expelled from a more massive neighbouring system (e.g. Ludlow et al. 2009; Li et al. 2013), or if their accretion was halted by tides from nearby structures (Wang et al. 2007; Hahn et al. 2009; Behroozi et al. 2013). Such tidal truncation of halo growth complicates the comparison of measured protohalo overdensities with the model-predicted thresholds in a couple of ways. First, the collapse redshift of the halo will coincide with the time at which mass accretion halted rather than the time at which the halo was identified, which raises the relevant model barrier by a factor $\sim D(z_{id})/D(z_c)$. Secondly, the tidal forces associated with strong interactions with neighbouring systems are not properly accounted for in the EC model. Such forces would inhibit collapse, further raising the threshold for halo formation. Incorporating such effects will likely require a substantial reform of the ellipsoidal model.

In Fig. 11 we provide a couple of visual examples of protohaloes in our $150 h^{-1}$ Mpc box that lie considerably above the collapse barrier inferred from our ECE model. The left-hand panels plot the linear density fields in the proto-

halo vicinity (smoothed on the mass scale of the halo) and panels on the right show their descendants in the evolved density fields. In each panel orange points show the particles that, at $z = 0$, belong to the FoF halo. Green points are those within a Lagrangian sphere centred on the protohalo that encloses a mean overdensity equivalent to the collapse threshold predicted by our ECE model (indicated by a thick green circle in each panel); these highlight the mass envisioned by EPS theory to collapse onto the halo by $z = 0$.

The first example, plotted in the top panels of Fig. 11, centres on a FoF halo of mass $\sim 4.2 \times 10^{12} h^{-1} M_\odot$; its predicted mass exceeds this value by nearly an order of magnitude. In the right hand panel it is clear that at $z = 0$ much of this mass is actually distributed amongst several haloes that trace a large-scale filamentary structure. The sets of light and dark blue points in each of the top panels show the locations of two neighbouring haloes that have accreted ~ 30 per cent of the mass that EPS would have associated with the central object. The centres of mass of these neighbouring protohaloes lie outside of the Lagrangian sphere of overdensity δ_{ec} , yet their own spheres (shown using blue circles) overlap with it. The remaining ~ 70 per cent of the mass is today distributed within other nearby haloes, or diffusely within the filamentary structure.

A similar example, shown in the lower panels of Fig. 11, centres on a FoF halo of mass of $M \sim 6.8 \times 10^{12} h^{-1} M_\odot$. Based on its linear overdensity (smoothed on the scale M), $\delta_h \approx 4.2$, EPS theory and the ellipsoidal barrier would have associated this halo with a mass $M_{ec} \sim 4.0 \times 10^{13} h^{-1} M_\odot$ (green points), roughly a factor of 6 larger than its true mass. The lower right-hand panel shows that much of this mass is, at $z = 0$, spread across a large, $\sim 10 h^{-1}$ Mpc filament. This tidal stretching of the linear perturbation is induced by two much larger neighbouring fluctuations, one with a mass of $\sim 3.5 \times 10^{14} h^{-1} M_\odot$ (light blue) and the other of $\sim 1.9 \times 10^{12} h^{-1} M_\odot$ (darker blue). Although these are distinct structures (their locations and Lagrangian sizes indicated using blue circles), together they accrete ~ 50 per cent of the total mass that *should* have collapsed upon the central halo.

Clearly the collapse of perturbations in Gaussian random fields is much more complex than what is envisioned by simple dynamical models, such as the SC or EC model. Fluctuations exist on a variety of spatial scales, and large-scale overdensities of different height and mass often overlap with one another. As a result, high density peaks capable of collapsing under their own self-gravity may strongly influence the evolution of neighbouring systems in ways that are not accounted for in the EC model. Extensions or refinements of the ellipsoidal model that incorporate the effects of non-linear tides, or attempt to model the unique assembly histories of DM haloes, may help reconcile the model predictions and the collapse dynamics of individual objects.

6 SUMMARY

We have used two cosmological simulations of structure formation to study the properties of the Lagrangian progenitors of CDM haloes (or “protohaloes”), the results of which were

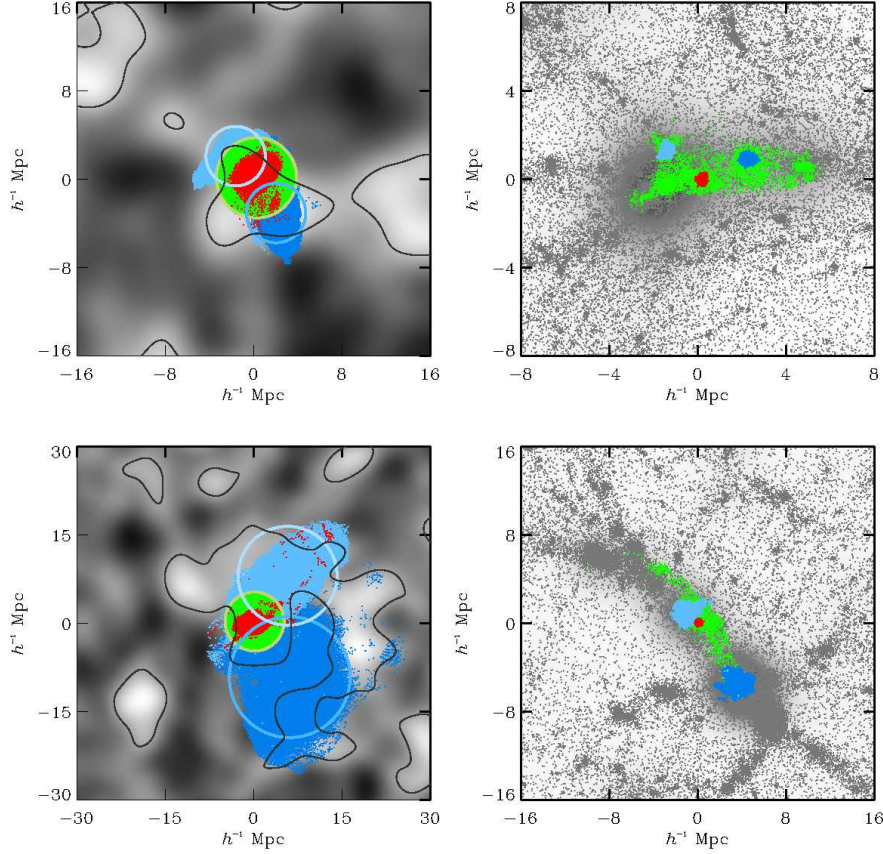


Figure 11. Red points show two examples of the Lagrangian (left) and Eulerian (right) locations of haloes whose linear density contrasts exceed the collapse threshold predicted by our ECE model for their measured initial shapes and external tides. Top panels correspond to a halo of mass $\sim 4.2 \times 10^{12} h^{-1} M_{\odot}$; bottom panels to a $\sim 6.8 \times 10^{12} h^{-1} M_{\odot}$ halo. In both left-hand panels, the linear density fields have been smoothed with a tophat filter scaled to the mass of the halo. Green points show the particles that fill a Lagrangian sphere, centred on each protohalo, whose mean density contrast is equal to the value predicted by our ECE model. Light and dark blue points show neighbouring protohaloes and their descendants whose growth substantially influences the collapse of the central object: these haloes generate strong tidal forces that strip matter from the central halo’s vicinity before it is able to accrete, thereby suppressing mass accretion on to the halo at early times. At $z = 0$, this material is distributed amongst several nearby haloes, or within filamentary structures in which the haloes form.

compared directly against the predictions of the EC model. Our main results can be summarized as follows.

- The Lagrangian patches that collapse to form CDM haloes that are identified at redshift z_{id} are, in general, non-spherical. Over the range of peak heights $0.6 \lesssim \nu \lesssim 4$, for example, the average minor-to-major axis ratio varies from roughly ~ 0.4 to ~ 0.7 , and fewer than 2 per cent of $\nu > 1$ haloes have a “sphericity” $q_3/q_1 > 0.8$.

- The non-spherical shapes of protohaloes are likely determined by the relative compression factors along their principal axes due the surrounding tidal field (see Fig. 5). For example, haloes that form in regions of the linear density field where λ_1 is large and positive, but λ_3 is large and negative, accrete mass from very flattened and elongated regions due to the differing gravitational tides along orthogonal directions. This results in a strong alignment between the principal axes of the inertia tensor of protohaloes and those of the linear tidal field (see also Lee & Pen 2000; Porciani et al. 2002).

- The average overdensity of DM protohaloes, δ_h , linearly extrapolated to their identification redshift, z_{id} , increases with the strength of the surrounding tidal field in a way that is described reasonably well by the classic EC model of BM96. At fixed mass, however, the scatter in δ_h depends strongly on the formation epoch, z_{50} , defined as the redshift at which half of its final mass was first assembled into one main progenitor. Furthermore, haloes that have collapsed very recently (for example, those with $t_{50}/t_{\text{id}} > 0.8$, where the t s are the corresponding cosmological times) tend to lie below the EC barrier but are neatly bounded beneath by the SC threshold, $\delta_{\text{sc}} \approx 1.686$, independent of the strength of their surrounding tidal field.

- This highlights a failure of the classic ellipsoidal model, which systematically over-predicts the density thresholds required for collapse to occur by z_{id} . This result can be explained by abandoning the model’s assumption that Lagrangian protohaloes are spherical. Allowing for initial asymmetry in the perturbation shape alters the collapse

times of its axes, resulting in a modification to the density threshold required for collapse to occur by a given time. When tuned to match the typical shapes of protohaloes in our simulation initial conditions, the modified ellipsoidal model accurately reproduces their minimum linear over-densities. EC models that assume initially spherical perturbations (BM96; Sheth et al. 2001) fail to describe the measured overdensities of protohaloes with non-spherical geometries.

- A caveat of our model is that the majority of protohaloes have $\delta_h(z_{id}) \geq \delta_{ec}(z_{id})$, suggesting that EPS theory (if executed using our collapse model) would substantially over-predict the masses of most haloes. We speculate that this is intimately related to differences between the hierarchical growth of CDM haloes and the simple collapse dynamics envisioned by ellipsoidal model. In particular, protohaloes that lie considerably above our model-predicted barrier tend to be highly clustered and reside in high-density regions, where overdensities on a variety of spatial scales likely overlap. The Lagrangian state of these systems therefore differs substantially from what is envisioned by simple models for the collapse of isolated density perturbations. Such complications are expected to affect halo collapse times, as well as the evolution of the tidal field acting upon each system, and therefore complicates a direct comparison of the model predictions to the outcome of numerical simulations. We will discuss these effects in more detail in a forthcoming paper.

Overall, our results indicate that the standard EC model (e.g. BM96; Sheth et al. 2001) provides a rather incomplete census of the possible collapse thresholds for the formation of DM haloes from Gaussian random fields. In addition to the specifics of the linear tidal field at a given location, the collapse threshold depends sensitively on the assumed shape of the Lagrangian region that eventually collapses to form a bound object, as well as on the its formation redshift. These results have important implications for understanding the origin of DM haloes; for modelling their assembly histories; as well as for interpreting the age-dependence of halo clustering.

ACKNOWLEDGMENTS

ADL acknowledges financial support from the Deutsche Forschungsgemeinschaft through the SFB (956), “The Conditions and Impact of Star Formation”, and MB through the Transregio 33, “The Dark Universe”. We thank Yehuda Hoffman and Ravi Sheth for useful discussions, and our referee, Aseem Paranjape, for a useful report which has improved this work.

APPENDIX A: A GENERAL ELLIPSOIDAL COLLAPSE MODEL

Following BM96, we consider a uniform density perturbation on top of a flat Friedmann-Robertson-Walker background whose energy content is dominated by the matter density, ρ_m , and a cosmological constant, Λ . We model the perturbation as a homogeneous ellipsoid with semi-axes of physical length r_i ($i = 1, 2, 3$) and density contrast, δ . We adopt a Cartesian coordinate system, x_i , that coincides with the

principal axes of the ellipsoid, which are also assumed to be perfectly aligned with the external tidal shear (see, e.g., Fig. 3).

In this coordinate system, the internal gravitational potential of the ellipsoid (which satisfies Poisson’s equation $\nabla^2 \phi = 4\pi G \rho_m (1 + \delta)$) can be written

$$\phi_{\text{ell}}(\mathbf{x}) = \pi G (1 + \delta) \rho_m \sum_{i=1}^3 b_i x_i^2, \quad (\text{A1})$$

where the coefficients b_i are given by Carlson’s elliptic integrals (Kellogg 1929; Chandrasekhar 1969):

$$b_i = r_1 r_2 r_3 \int_0^\infty \frac{d\tau}{(\tau + r_i^2) \prod_{j=1}^3 (\tau + r_j^2)^{1/2}}. \quad (\text{A2})$$

The potential generated by the uniform distribution of matter outside the perturbation is given by

$$\phi(\mathbf{x}) = \pi G \rho_m \sum_{i=1}^3 \left(\frac{2}{3} - b_i \right) x_i^2 - \frac{\Lambda c^2}{6} \sum_{i=1}^3 x_i^2. \quad (\text{A3})$$

The first term in this expression is the external potential generated by the perturbation itself. It is obtained by considering the superposition of a uniform matter distribution and an ellipsoidal “hole” with a density of $-\rho_m$. The second term in equation (A3) is the contribution from the cosmological constant. The total gravitational potential is thus given by

$$\phi(\mathbf{x}) = \pi G \rho_m \sum_{i=1}^3 \left([(1 + \delta) b_i - \beta_i] - \frac{\Lambda c^2}{6} \right) x_i^2, \quad (\text{A4})$$

where we have used $\beta_i = b_i - 2/3$.

Assuming that the tidal shear is parallel to the principal axes of the density perturbation (which naturally arises when one starts with a sheared spherical perturbation), we can write the equation of motion for the semi-axis lengths r_i of the ellipsoid as

$$\frac{\ddot{r}_i}{r_i} = \frac{\Lambda c^2}{3} - 4\pi G \rho_m \left(\frac{1 + \delta}{3} + \frac{\beta_i}{2} \delta + \lambda_i^{\text{ext}} \right), \quad (\text{A5})$$

where dots denote time derivatives and we have used the fact that $b_i (1 + \delta) - \beta_i = \beta_i \delta + 2(1 + \delta)/3$.

Because the potential is quadratic and the acceleration is linear in the coordinates, concentric ellipsoids with the same axis ratios evolve self-similarly and the density perturbation remains homogeneous at all times. Given the comoving coordinates of the axes extrema, q_i , the evolution thus preserves $r_1 r_2 r_3 (1 + \delta) = q_1 q_2 q_3 a^3 = \text{constant}$, and the overdensity of the perturbation evolves as

$$\delta(a) = \frac{q_1 q_2 q_3}{r_1 r_2 r_3} a^3 - 1. \quad (\text{A6})$$

Initial conditions for equation (A5) can be set according to the Zel’dovich approximation at some early time, t_0 :

$$r_i(t_0) = q_i [1 - \lambda_i(t_0)] a(t_0), \quad (\text{A7})$$

$$\dot{r}_i(t_0) = H(t_0) r_i(t_0) - q_i H_D(t_0) \lambda_i(t_0) a(t_0). \quad (\text{A8})$$

Here $H = \dot{a}/a$ is the Hubble parameter; D the linear growth factor; $H_D \equiv \dot{D}/D$, and $\lambda_i(t) \propto D(t)$ are the eigenvalues of the linear deformation tensor. In order to match the last expressions with equation (A5), we also derive the eigenvalues

of the deformation tensor at t_0 from the peculiar gravitational potential (which satisfies $\nabla^2 \Phi = \delta$):

$$\begin{aligned}\lambda_i^{\text{tot}}(t_0) &= \frac{\delta(t_0)}{2} b_i(t_0) + \lambda_i^{\text{ext}}(t_0) \\ &= \delta(t_0) \left(\frac{1}{3} + \frac{\beta_i(t_0)}{2} \right) + \lambda_i^{\text{ext}}(t_0).\end{aligned}\quad (\text{A9})$$

Only the components of this expression that scale as $D(t)$ will contribute to the λ_i terms appearing in the Zel'dovich approximation.

The early evolution of the internal gravitational potential of the ellipsoid can be determined by combining equation (A2) and (A7) and Taylor expanding in powers of $D(t)$:

$$\beta_i(t) = \beta_i^{(0)} + \Delta\beta_i D(t) + \mathcal{O}[D^2(t)]. \quad (\text{A10})$$

Here $\beta_i^{(0)}$ is evaluated using equation (A2) with $r_i = q_i$, and the second term in is given by

$$\Delta\beta_i D(t) = \sum_{j=1}^3 \alpha_{ij} \lambda_j, \quad (\text{A11})$$

where

$$\alpha_{jj} = q_1 q_2 q_3 \int_0^\infty \frac{(2q_j^2 - \tau) d\tau}{(q_j^2 + \tau)^2 \prod_{i=1}^3 (q_i^2 + \tau)^{1/2}} \quad (\text{A12})$$

and, for $j \neq i$,

$$\alpha_{ji} = -q_1 q_2 q_3 \int_0^\infty \frac{\tau d\tau}{(q_j^2 + \tau)(q_i^2 + \tau) \prod_{i=1}^3 (q_i^2 + \tau)^{1/2}}, \quad (\text{A13})$$

When all q_i s are equal $\alpha_{ij} = 8/15$ for $i = j$ and $-4/15$ when $i \neq j$ and this reduces to the result of BM96, $\beta_i \simeq \Delta\beta_i D(t) = (4/5) t_i$. Thus, the term $\beta \delta/2$ in equation (A10) is of second order in $D(t)$ and does not contribute to the linear shear tensor, which is fully generated by the external tides. For initially triaxial perturbations, however, the linear velocity shear is composed of two terms:

$$\lambda_i = \frac{\delta}{3} + \left[\frac{\beta_i^{(0)} \delta}{2} + \lambda_i^{\text{ext}} \right]. \quad (\text{A14})$$

For the typical axes ratios of protohaloes in our simulations ($q_2/q_1 \simeq q_3/q_2 \simeq 0.8$) we find $\beta_i^{(0)} \simeq (-0.170, -0.011, 0.182)$, showing that internal shear slows down collapse along the long axis and speeds it up along the short axis.

Solving equation (A5) requires knowledge of the time evolution of the external tidal field, λ_i^{ext} . BM96 proposed two limiting approximations. In one case, the external tides are assumed to grow independently of the ellipsoid and the shear scales as the linear growth factor,

$$\lambda_i^{\text{ext}}(t) = \frac{D(t)}{D(t_0)} \lambda_i^{\text{ext}}(t_0). \quad (\text{A15})$$

Alternatively, one can assume that the external shear is dominated by the shape of the ellipsoid itself. In this case, $\lambda_i^{\text{ext}}(t) = (5/4) \beta_i$ (note that this reduces to equation (A15) at early times), or, more generally for triaxial perturbations,

$$\lambda_i^{\text{ext}}(t) = \sum_j \alpha_{ij}^{-1} (\beta_j - \beta_j^{(0)}), \quad (\text{A16})$$

where the α_{ij}^{-1} are the elements of the inverse matrix of α_{ij} . A hybrid model which interpolates between these asymptotic regimes has been recently proposed by Angrick & Bartelmann (2010). Here one uses the non-linear growth proposed by BM96 until the corresponding axis turns around and linear growth is used afterward.

Finally, the equations of motion for the axis lengths do not account for the physics of virialization. Relaxation processes are instead mimicked by “freezing” collapse along each axis once a critical radius $r_{\text{eq},i} = f a q_i$ is reached. BM96 suggested using the radial freeze-out factor $f = 0.178$, which results in a virial density contrast of ~ 178 in the SC model; this value is also commonly adopted in applications of the EC model. More recently, Angrick & Bartelmann (2010) used the tensor virial theorem to predict more realistic values of f . However, the last phase of collapse is generally rapid, and altering the value of f does not strongly affect the estimated epoch of virialization. For ease of comparison with previous work, all applications of this model presented in this paper have assumed a freeze-out factor $f = 0.178$.

REFERENCES

- Angrick C., Bartelmann M., 2010, *A&A*, 518, A38+
- Bailin J., Steinmetz M., 2005, *ApJ*, 627, 647
- Bardeen J. M., Bond J. R., Kaiser N., Szalay A. S., 1986, *ApJ*, 304, 15
- Behroozi P. S., Wechsler R. H., Lu Y., Hahn O., Busha M. T., Klypin A., Primack J. R., 2013, *ArXiv e-prints*
- Bett P., Eke V., Frenk C. S., Jenkins A., Helly J., Navarro J., 2007, *MNRAS*, 376, 215
- Bond J. R., Cole S., Efstathiou G., Kaiser N., 1991, *ApJ*, 379, 440
- Bond J. R., Myers S. T., 1996, *ApJS*, 103, 1
- Catelan P., Matarrese S., Porciani C., 1998, *ApJL*, 502, L1+
- Catelan P., Theuns T., 1996, *MNRAS*, 282, 455
- Chandrasekhar S., 1969, *Ellipsoidal figures of equilibrium*
- Cole S., Lacey C., 1996, *MNRAS*, 281, 716
- Dalal N., White M., Bond J. R., Shirokov A., 2008, *ApJ*, 687, 12
- Despali G., Giocoli C., Tormen G., 2014, *ArXiv e-prints*
- Despali G., Tormen G., Sheth R. K., 2013, *MNRAS*, 431, 1143
- Doroshkevich A. G., 1970, *Astrofizika*, 6, 581
- Eisenstein D. J., Loeb A., 1995, *ApJ*, 439, 520
- Eke V. R., Cole S., Frenk C. S., 1996, *MNRAS*, 282, 263
- Elia A., Ludlow A. D., Porciani C., 2012, *MNRAS*, 421, 3472
- Hahn O., Paranjape A., 2014, *MNRAS*, 438, 878
- Hahn O., Porciani C., Dekel A., Carollo C. M., 2009, *MNRAS*, 398, 1742
- Heavens A., Peacock J., 1988, *MNRAS*, 232, 339
- Icke V., 1973, *A&A*, 27, 1
- Kauffmann G., White S. D. M., 1993, *MNRAS*, 261, 921
- Kellogg O. D., 1929, *Foundations of Potential Theory*
- Komatsu E., Dunkley J., Nolte M. R., Bennett C. L., Gold B., Hinshaw G., Jarosik N., Larson D., Limon M., Page L., Spergel D. N., Halpern M., Hill R. S., Kogut A., Meyer S. S., Tucker G. S., Weiland J. L., Wollack E., Wright E. L., 2009, *ApJS*, 180, 330

- Lacey C., Cole S., 1993, MNRAS, 262, 627
 Lee J., Pen U., 2000, ApJL, 532, L5
 Lemson G., 1993, MNRAS, 263, 913
 Li R., Gao L., Xie L., Guo Q., 2013, MNRAS, 435, 3592
 Lin C. C., Mestel L., Shu F. H., 1965, ApJ, 142, 1431
 Ludlow A. D., Navarro J. F., Springel V., Jenkins A., Frenk C. S., Helmi A., 2009, ApJ, 692, 931
 Ludlow A. D., Porciani C., 2011, MNRAS, 413, 1961
 Lynden-Bell D., 1964, ApJ, 139, 1195
 Mo H. J., Jing Y. P., White S. D. M., 1997, MNRAS, 284, 189
 Mo H. J., White S. D. M., 1996, MNRAS, 282, 347
 Peebles P. J. E., 1980, The large-scale structure of the universe
 Pillepich A., Porciani C., Hahn O., 2010, MNRAS, 402, 191
 Porciani C., Dekel A., Hoffman Y., 2002, MNRAS, 332, 339
 Porciani C., Matarrese S., Lucchin F., Catelan P., 1998, MNRAS, 298, 1097
 Press W. H., Schechter P., 1974, ApJ, 187, 425
 Robertson B. E., Kravtsov A. V., Tinker J., Zentner A. R., 2009, ApJ, 696, 636
 Sheth R. K., Lemson G., 1999a, MNRAS, 304, 767
 Sheth R. K., Lemson G., 1999b, MNRAS, 305, 946
 Sheth R. K., Mo H. J., Tormen G., 2001, MNRAS, 323, 1
 Sheth R. K., Tormen G., 2002, MNRAS, 329, 61
 van den Bosch F. C., 2002, MNRAS, 331, 98
 Wang H. Y., Mo H. J., Jing Y. P., 2007, MNRAS, 375, 633
 Watanabe T., Inagaki S., 1991, PASJ, 43, 413
 White S. D. M., 1996, in Schaefer R., Silk J., Spiro M., Zinn-Justin J., eds, Cosmology and Large-Scale Structure Formation and evolution of galaxies: Les houches lectures. Dordrecht: Elsevier, astro-ph/9410043
 White S. D. M., Silk J., 1979, ApJ, 231, 1